Journal of Applied Electrochemistry **31**: 145–154, 2001.

Two-dimensional two-phase numerical model for tool design in electrochemical machining

C.S. CHANG and L.W. HOURNG
Department of Mechanical Engineering, National Central University, Chung-Li, Taiwan 32054

Received 10 January 2000; accepted in revised form 22 August 2000

Key words: ECM, inverse problem, numerical, two-phase flow

Abstract

Tool design in electrochemical machining is investigated including the effects of thermal-fluid properties of the electrolyte. A two-dimensional two-phase numerical model is used to predict the thermal-fluid field. Simulation indicates that, as the curvature of the electrode shape varies widely, the two-dimensional phenomenon of the flow is apparent and the two-dimensional model should be used during the numerical simulation. In addition, a higher electrolyte flow rate slightly reduces the two-dimensional effects. As the curvature of the electrode shape varies only slightly, one-dimensional analysis is accurate and capable of reducing the calculation time.

List of symbols

C_D	drag coefficient
C_l	specific heat of electrolyte (J kg^{-1} K^{-1})
d_b	bubble diameter (m)
$\vec{E}$	electrical intensity (V m^{-1})
Fr	Froude number
f_r	feed rate of the tool (m s^{-1})
$f(x)$	given tool shape
g	electrode gap (m)
g_e	equilibrium gap thickness at inlet (m)
$h(x)$	workpiece shape
J, $\vec{J}$	current density (A cm^{-2})
J_a	Jacobian
K_e	electrical conductivity of electrolyte (Ω^{-1} m^{-1})
k_l	thermal conductivity of electrolyte (W m^{-1} K^{-1})
M_{ij}	momentum source associated with a transfer of mass
n	unit normal of a surface
P	pressure (Pa)
Pr	Prandtl number
q	pressure correction
Re	Reynolds number
$r(x)$	required workpiece shape
T	electrolyte temperature (K)
u, v	velocity of electrolyte flow (m s^{-1})
V_A	velocity of anode dissolution (m s^{-1})
V_C	velocity of cathode (m s^{-1})
W	energy generation rate (W m^{-2})

Greek symbols

Γ	net mass source rate per unit volume (kg m^{-3} s^{-1})
α	volume fraction
γ	conductance constant, Equation 7 (K^{-1})
θ	angle (see Figure 1)
Λ	current efficiency
λ_a	electrochemical equivalent (g C^{-1})
μ	viscosity coefficient (kg m^{-1} s^{-1})
ρ	density (kg m^{-3})
ϕ	electric potential (V)
ϕ_a	applied voltage (V)

Subscripts

0	condition at entrance of electrolyte
a	anode
c	cathode
e	exit condition
l	liquid phase
g	gas phase

Superscripts

0	dimensionless parameter
k	iteration counter
m	generalization of heterogeneous conduction mechanism, Equation 7

1. Introduction

Conventionally used in diverse industries such as aerospace, nuclear and automotive, electrochemical machining (ECM) uses anodic dissolution to machine complex shapes and difficult-to-machine materials at high material removal rates, with good surface finish, without residual stresses and without damage to the microstructure of a workpiece [1, 2]. ECM connects the workpiece (anode) to the tool (cathode) via an electrolytic cell,

through which, an electrolyte is pumped to carry away the dissolved metal at the anode surface and the hydrogen produced at the cathode surface.

The tool design in ECM consists of two methods: direct and inverse. The direct method refers to the conventional analysis of anode shape evolution resulting from a specified tool shape. Analytic techniques include the $\cos\theta$ method [3], the analogue method [4] and the complex variables method [5]. Various numerical techniques, including the finite difference method [6, 7] and the finite element method (FEM) [8], have also been applied. However, the above do not consider the effects of many important parameters such as the mode of electrolyte flow on ECM and change in the electrolyte electrical conductivity. Thorpe and Zerkle [9, 10] proposed a one-dimensional, two-phase fluid flow model, demonstrating that most ECM can be treated as a quasi-steady process. Jain et al. [11] simulated ECM processes in which electric and flow fields affect the metal removal rate. Hourng solved one-dimensional, bubbly two-phase [12] and a two-dimensional, one-phase [13] flow field to accurately predict the workpiece shape and the variations of electrolyte properties between electrodes.

A more direct approach to ECM tool design is by solution of the inverse method in which the admissible tool shapes are determined directly from the given workpiece geometry. Among the algorithms proposed in recent years include the boundary element method [14], the complex variables method [15], multigrid techniques [16] and the embedding method [17]. Although these approaches are highly effective for smooth, two-dimensional anode shapes, to our knowledge, no extensions have been made to explain the effect of the thermal-fluid properties on electrolyte electrical conductivity. Chang, Hourng and Chung [18] considered the effect of thermal-fluid properties with a one-dimensional bubbly-two-phase flow model to accurately predict the tool shape for a given workpiece shape. However, the simulation of the fluid field is a one-dimensional model and inadequate for an electrode with an abrupt shape. Multi-dimensional analysis is necessary to accurately model the local distributions of flow and temperature in which the shapes of cathode and anode are complex.

This study investigates the effectiveness of the inverse method in ECM, particularly with respect to the effect of thermal-fluid properties. A finite Fourier series, constructed from even and odd harmonics, is used in the electrode representation to reduce the relative errors. In addition, the two-dimensional electric potential field is solved and a two-dimensional two-phase model is used to simulate the flow field during electrochemical machining. The variations of velocity, pressure, temperature and volume fraction of the hydrogen gas phase and the electrolyte liquid phase are demonstrated and analysed in detail. More thoroughly understanding of the machining conditions and the numerical parameters facilitates the design of the tool shape, especially for abrupt electrode shapes. Simulation indicates that the workpiece shape machined by the predicted tool correlates well with the required work piece shape.

2. Theoretical model

2.1. *Electric field and variation of interelectrode gap*

Consider a two-dimensional electrochemical machining problem as illustrated in Figure 1. In steady state situations, conservation of charge gives $\nabla \cdot \vec{J} = 0$, where $\vec{J}$ is the electric current density. According to Ohms law, $\vec{J} = -K_e \nabla \phi$, where ϕ is the electric potential and K_e is the electrolyte electrical conductivity. The governing equation and boundary conditions for the model are as follows:

$$\nabla \cdot (K_e \nabla \phi) = 0 \tag{1}$$

$$\left.\begin{array}{ll} \text{(i) the anode surface } \overline{AB}: & \phi = \phi_a \\ \text{(ii) the cathode surface } \overline{DC}: & \phi = 0 \\ \text{(iii) the flow inlet } \overline{AD}: & \frac{\partial \phi}{\partial n} = 0 \\ \text{(iv) the flow exit } \overline{BC}: & \frac{\partial \phi}{\partial n} = 0 \end{array}\right\} \tag{2}$$

where ϕ_a is the applied voltage. Boundary conditions 2(iii) and 2(iv) indicate that no current flows across the inlet/outlet which should be $\partial\phi/\partial n = 0$ since n refers to the normal tool/workpiece surfaces. The electrode gap, g, is measured perpendicularly to the workpiece and varied as

$$\frac{\partial g}{\partial t} = V_A - V_C \tag{3}$$

where V_C is the local cathode feed velocity, and V_A is the dissolution velocity of the anode in the direction normal to the tool surface. Based on Ohm's law and Faraday's law, Equation 3 can be written as

$$\frac{\partial g}{\partial t} = \frac{\Lambda \lambda_a J}{\rho_a} - f_r \cos\theta \tag{4}$$

where λ_a is the electrochemical equivalent, Λ the current efficiency, ρ_a the anode density, f_r the feed rate of the tool and θ the angle between the outer normal of the workpiece and the feed direction as shown in Figure 1. The equilibrium gap thickness at inlet, g_e, can be expressed as

$$g_e = \frac{\Lambda \lambda_a K_e}{\rho_a} \frac{\phi_a}{f_r} \tag{5}$$

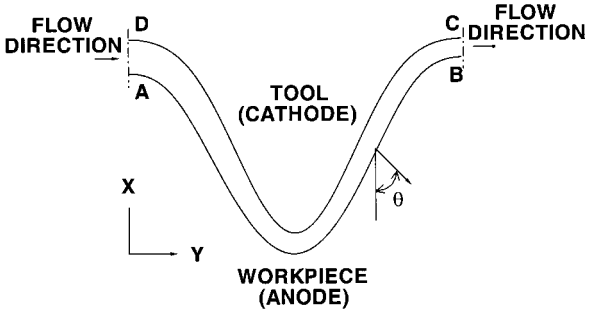

Fig. 1. A typical ECM configuration.

The current density normal to the workpiece, J, as described above is

$$J = K_{\mathrm{e}} \frac{\partial \phi}{\partial n} \tag{6}$$

where n is the unit normal of the workpiece surface, and the electrolyte electrical conductivity can be represented [9] by

$$K_{\mathrm{e}} = K_{\mathrm{e}0}(1-\alpha_g)^m[1+\gamma(T-T_0)] \tag{7}$$

where the zero subscript denotes the condition at the entrance of the electrode gap, γ the conductance constant, and T the electrolyte temperature. In addition, exponent m is a generalization of heterogeneous conduction mechanism and is taken to be 1.75 [9]. For a one-dimensional model, the void fraction is defined as

$$\alpha_g = \frac{g_g}{g} \tag{8}$$

where g_g denotes the dimension occupied by the gas phase. For the two-dimensional two-phase model α_g is the volume fraction occupied by the gas phase.

2.2. *Fluid equations*

If the curvature of the electrode shape varies widely, the electrolyte flow is two-dimensional. Then, the two-dimensional, two-phase model is required to simulate the distributions of the thermal-fluid properties. The flow in the interelectrode gap contains the electrolyte liquid phase and the hydrogen gas phase. In the current application, the electrolyte velocity in the interelectrode gap is not very fast ($\ll 0.3\ M_{\mathrm{a}}$, Mach number) and the variation of the temperature is slight. For convenience of analysis, the flow is thus assumed to be quasi-steady, incompressible and laminar. The equations describing the conservation of mass and linear momentum of the ith component are given by Equations 9, 10 and 11.

$$\frac{\partial}{\partial t}(\alpha_i\rho_i) + \frac{\partial}{\partial x}(\alpha_i\rho_i u_i) + \frac{\partial}{\partial y}(\alpha_i\rho_i v_i) = \Gamma_i \tag{9}$$

$$\begin{aligned}\frac{\partial}{\partial t}(\alpha_i\rho_i u_i) &+ \frac{\partial}{\partial x}(\alpha_i\rho_i u_i u_i) + \frac{\partial}{\partial y}(\alpha_i\rho_i u_i v_i) \\ &= -\alpha_i\frac{\partial P}{\partial x} + b_{xi} + \frac{\partial}{\partial x}\left(\alpha_i\mu_i\frac{\partial u_i}{\partial x}\right) + \frac{\partial}{\partial y}\left(\alpha_i\mu_i\frac{\partial u_i}{\partial y}\right) \\ &\quad + f_x(u_j-u_i) + M_{ij_x}\end{aligned} \tag{10}$$

$$\begin{aligned}\frac{\partial}{\partial t}(\alpha_i\rho_i v_i) &+ \frac{\partial}{\partial x}(\alpha_i\rho_i v_i u_i) + \frac{\partial}{\partial y}(\alpha_i\rho_i v_i v_i) \\ &= -\alpha_i\frac{\partial P}{\partial y} + b_{yi} + \frac{\partial}{\partial x}\left(\alpha_i\mu_i\frac{\partial v_i}{\partial x}\right) + \frac{\partial}{\partial y}\left(\alpha_i\mu_i\frac{\partial v_i}{\partial y}\right) \\ &\quad + f_y(v_j-v_i) + M_{ij_y}\end{aligned} \tag{11}$$

where $i = 1, 2$ with $j = 3 - i$, α_i is the volume fraction occupied by component i, ρ_i is the density of this component in its pure state, $\mathbf{v}_i = (u_i, v_i)$ is the velocity vector, and Γ_i is the net mass source rate per unit volume due to the electrochemical reaction. Faraday's law of the electrolysis can be used to determine the rate of dissolution of the hydrogen gas near the cathode. Moreover, P is the common pressure, μ_i is the coefficient of viscosity, and $\mathbf{b} = (b_{xi}, b_{yi})$ is the gravity term. Since the x direction is perpendicular to the gravity direction, b_{xi} is equal to zero, and $b_{yi} = \alpha_i(\rho_j - \rho_i)g$. $\mathbf{f} = (f_x, f_y)$ is coefficient for the inter-phase frictional forces. Where $\mathbf{M}_{ij} = (M_{ij_x}, M_{ij_y})$ is the momentum source associated with the mass transfer between components i and j.

In addition to the differential equations, the following algebraic auxiliary relations are needed. Herein, the flow in the interelectrode gap containing only the liquid electrolyte phase and the hydrogen gas phase is assumed since the amount of the solid material absorbed from the workpiece is small. Thus, there is no net source of mass, and the mass source rates must satisfy Equation 12.

$$\sum_i \Gamma_i = 0 \tag{12}$$

The relationship between the volume fractions can be expressed as

$$\sum_i \alpha_i = 1 \tag{13}$$

The friction-force coefficients $\mathbf{f} = (f_x, f_y)$ are determined by

$$\mathbf{f} = \tfrac{1}{2}\mathbf{C}_{\mathrm{D}}\rho_l\left|\mathbf{v}_j - \mathbf{v}_i\right|/d_{\mathrm{b}} \tag{14}$$

where d_{b} is the bubble diameter taken to be 100 μm here [1]. $\mathbf{C}_{\mathrm{D}} = (C_{\mathrm{Dx}}, C_{\mathrm{Dy}})$ is the drag coefficient obtained from appropriate empirical relations. In current applications, the flow is laminar, and $\mathbf{C}_{\mathrm{D}}$ is determined by the following formula [19]:

$$\mathbf{C}_{\mathrm{D}} = \frac{6.3}{\mathbf{Re}_{\mathrm{b}}^{0.385}} \tag{15}$$

and $\mathbf{Re}_{\mathrm{b}} = \frac{\rho_l|\mathbf{v}_j - \mathbf{v}_i|d_{\mathrm{b}}}{\mu_l}$. Note that $\mathbf{Re}_{\mathrm{b}} = (Re_{bx}, Re_{by})$, $\mathbf{v} = (u, v)$, and subscripts l and g denote the liquid phase and the gas phase, respectively.

Dimensionless parameters are defined as follows:

$$\begin{aligned} &x^0 = x/g_{\mathrm{e}}, \quad y^0 = y/g_{\mathrm{e}}, \quad u_i^0 = u_i/u_0, \\ &v_i^0 = v_i/u_0, \quad \mu_i^0 = \mu_i/\mu_l, \quad \rho_i^0 = \rho_i/\rho_l, \\ &t^0 = \frac{t}{g_{\mathrm{e}}/u_0}, \quad P^0 = \frac{P - P_{\mathrm{e}}}{\rho_l u_0^2} \end{aligned}$$

where the zero superscript denotes the dimensionless parameter, the zero subscript denotes the condition at the entrance, and P_{e} the exit pressure.

Equations 9, 10 and 11 can be rewritten as

$$\frac{\partial}{\partial t^0}\left(\alpha_i\rho_i^0\right)+\frac{\partial}{\partial x^0}\left(\alpha_i\rho_i^0u_i^0\right)+\frac{\partial}{\partial y^0}\left(\alpha_i\rho_i^0v_i^0\right)=\Gamma_i^0 \tag{16}$$

$$\begin{aligned}&\frac{\partial}{\partial t^0}\left(\alpha_i\rho_i^0u_i^0\right)+\frac{\partial}{\partial x^0}\left(\alpha_i\rho_i^0u_i^0u_i^0\right)+\frac{\partial}{\partial y^0}\left(\alpha_i\rho_i^0u_i^0v_i^0\right)\\&\quad=-\alpha_i\frac{\partial P^0}{\partial x^0}+\frac{1}{Re}\left[\frac{\partial}{\partial x^0}\left(\alpha_i\mu_i^0\frac{\partial u_i^0}{\partial x^0}\right)+\frac{\partial}{\partial y^0}\left(\alpha_i\mu_i^0\frac{\partial u_i^0}{\partial y^0}\right)\right]\\&\qquad+f_x^0\left(u_j^0-u_i^0\right)+M_{ij_x}^0\end{aligned} \tag{17}$$

$$\begin{aligned}&\frac{\partial}{\partial t^0}\left(\alpha_i\rho_i^0v_i^0\right)+\frac{\partial}{\partial x^0}\left(\alpha_i\rho_i^0v_i^0u_i^0\right)+\frac{\partial}{\partial y^0}\left(\alpha_i\rho_i^0v_i^0v_i^0\right)\\&\quad=-\alpha_i\frac{\partial P^0}{\partial y^0}+\frac{1}{Re}\left[\frac{\partial}{\partial x^0}\left(\alpha_i\mu_i^0\frac{\partial v_i^0}{\partial x^0}\right)+\frac{\partial}{\partial y^0}\left(\alpha_i\mu_i^0\frac{\partial v_i^0}{\partial y^0}\right)\right]\\&\qquad+f_y^0\left(v_j^0-v_i^0\right)+\frac{1}{Fr^2}\alpha_j\left(\rho_j^0-\rho_i^0\right)+M_{ij_y}^0\end{aligned} \tag{18}$$

where $\Gamma_i^0=\Gamma_i g_e/\rho_l u_0$, Re (the Reynolds number) $=\rho_l u_0 g_e/\mu_l$, Fr^2 (the Froude number) $=u_0^2/g_e g$, $\mathbf{f}^0=\mathrm{f}g_e/\rho_l u_0$ and $\mathbf{M}_{ij}^0=\mathbf{M}_{ij}g_e/\rho_l u_0^2$.

Equations 16, 17 and 18 can be rewritten in an abbreviated form and the superscript 0 can be omitted for clarity as

$$\frac{\partial}{\partial t}\alpha_i+\nabla\cdot(\alpha_i\mathbf{v}_i)=\frac{\Gamma_i}{\rho_i} \tag{19}$$

and

$$\frac{\partial}{\partial t}(\rho_i\alpha_i\mathbf{v}_i)+A(\mathbf{v}_i)=-\alpha_i(\nabla\cdot P)+\frac{\mu_i}{Re}\boldsymbol{\tau}_i+\mathbf{S}_i \tag{20}$$

where

$$A(\mathbf{v}_i)=\left(\left[\frac{\partial}{\partial x}(\alpha_i\rho_i u_i u_i)+\frac{\partial}{\partial y}(\alpha_i\rho_i u_i v_i)\right],\left[\frac{\partial}{\partial x}(\alpha_i\rho_i v_i u_i)+\frac{\partial}{\partial y}(\alpha_i\rho_i v_i v_i)\right]\right)$$

$$\boldsymbol{\tau}_i=\left(\left[\frac{\partial}{\partial x}\left(\alpha_i\mu_i\frac{\partial u_i}{\partial x}\right)+\frac{\partial}{\partial y}\left(\alpha_i\mu_i\frac{\partial u_i}{\partial y}\right)\right],\left[\frac{\partial}{\partial x}\left(\alpha_i\mu_i\frac{\partial v_i}{\partial x}\right)+\frac{\partial}{\partial y}\left(\alpha_i\mu_i\frac{\partial v_i}{\partial y}\right)\right]\right)$$

$$\mathbf{S}_i=\left(\lfloor f_x(u_j-u_i)+M_{ij_x}\rfloor,\left[f_y(v_j-v_i)+\frac{1}{Fr^2}\alpha_j(\rho_j-\rho_i)+M_{ij_y}\right]\right)$$

Since the flow field is assumed to be a quasi-steady state, the independent derivative t in the above fluid equations is not the actual time but the fictitious time of the iteration step in the numerical scheme.

The incompressible two-phase Navier–Stokes equations, (Equations 19 and 20) are nonlinear and solved here as follows [20]. If the velocity field at iteration step $n+1$ is to be determined by the known velocity field at iteration step n, an intermediate velocity field $(\alpha_i\mathbf{v}_i)^*$ is initially obtained from Equation 20 by using the values at iteration step n, that is,

$$\begin{aligned}&\rho_i\frac{(\alpha_i\mathbf{v}_i)^*-(\alpha_i\mathbf{v}_i)^n}{\delta t}+A(\mathbf{v}_i)^n\\&\quad=-\alpha_i^n(\nabla\cdot P^n)+\frac{\mu_i}{Re}\boldsymbol{\tau}_i+\mathbf{S}_i\end{aligned} \tag{21}$$

The velocity field at iteration step $n+1$, $(\alpha_i\mathbf{v}_i)^{n+1}$, is then obtained by

$$\rho_i\frac{(\alpha_i\mathbf{v}_i)^{n+1}-(\alpha_i\mathbf{v}_i)^*}{\delta t}=-\alpha_i^n(\nabla\cdot q) \tag{22}$$

where q is a pressure correction. The pressure correction must first be determined before applying Equation 22. Taking the divergence of Equation 22 leads to

$$\nabla\cdot\left[(\alpha_i\mathbf{v}_i)^{n+1}-(\alpha_i\mathbf{v}_i)^*\right]=-(\delta t)\nabla\cdot\left(\frac{\alpha_i^n}{\rho_i}\nabla\cdot q\right) \tag{23}$$

The final velocities at iteration step $n+1$ must satisfy Equation 19, that is,

$$\nabla\cdot(\alpha_i\mathbf{v}_i)^{n+1}=\frac{\Gamma_i}{\rho_i}-\frac{\partial}{\partial t}\alpha_i \tag{24}$$

Substituting Equation 24 into Equation 23 and then summing over all phases yields

$$\begin{aligned}&\nabla\cdot\left[\left(\sum_i\frac{\alpha_i^n}{\rho_i}\right)(\nabla\cdot q)\right]\\&\quad=\frac{1}{\delta t}\left\{\nabla\cdot\left[\sum_i(\alpha_i\mathbf{v}_i)^*\right]-\sum_i\frac{\Gamma_i}{\rho_i}\right\}\end{aligned} \tag{25}$$

The derivative term has vanished owing to

$$\sum_i\frac{\partial}{\partial t}(\alpha_i)=\frac{\partial}{\partial t}\left(\sum_i\alpha_i\right)=\frac{\partial}{\partial t}(1)=0$$

Equation 25, a Poisson like equation, is solved for the pressure correction q.

The volume fraction can then be obtained from Equation 24, that is,

$$\alpha_i^{n+1}=\alpha_i^n+\delta t\left[\frac{\Gamma_i}{\rho_i}-\nabla\cdot(\alpha_i\mathbf{v}_i)^{n+1}\right] \tag{26}$$

The above iteration is repeated until the convergence criteria are satisfied.

The boundary conditions deemed necessary to solve the flow field are described as follows. The pressure at exit is given and the pressures along other boundaries are calculated by the projection method [21]. Since the governing equations for the velocity field are elliptic, the velocity at the inlet and exit planes is needed to ensure mathematic exactness.

Therefore, the velocity distribution of the flow at the inlet and the exit planes are assumed to be uniform and fully developed, respectively. The fully developed boundary condition at the outlet is dictated by the flow if the duct near the outlet is flat and extends for a long distance.

2.3. *Thermal field*

Since the mass of the hydrogen gas during the ECM process is very small, for the convenience of thermal field analysis, the unequal velocity equal temperature (UVET) model is used to simulate the flow in the interelectrode gap. Furthermore, the energy dissipation can be neglected since the electrolyte velocity and the corresponding Eckert number are small. By using the inlet temperature of the electrolyte as the characteristic temperature, the dimensionless form of the energy equation is

$$(\rho u)_m^0 \frac{\partial T^0}{\partial x^0} + (\rho v)_m^0 \frac{\partial T^0}{\partial y^0} = \frac{1}{PrRe}\left(\frac{\partial^2 T^0}{\partial x^{0^2}} + \frac{\partial^2 T^0}{\partial y^{0^2}}\right) + W^0 \quad (27)$$

where $(\rho u)_m^0$ and $(\rho v)_m^0$ are the dimensionless flow rates of the two-phase mixture in x- and y-directions, respectively, and determined by

$$(\rho u)_m^0 = \frac{\alpha_g \rho_g u_g + \alpha_l \rho_l u_l}{\rho_l u_0} \quad (28)$$

and

$$(\rho v)_m^0 = \frac{\alpha_g \rho_g v_g + \alpha_l \rho_l v_l}{\rho_l u_0} \quad (29)$$

and Pr (Prandtl number) $= \mu_l C_l / k_l$ and $W^0 = W g_e / (\rho_l C_l T_0 u_0)$, where W, the energy generation rate originating from the current, can be obtained by the Joule law as

$$W = \vec{E} \cdot \vec{J} = K_e \left[\left(\frac{\partial \phi}{\partial x}\right)^2 + \left(\frac{\partial \phi}{\partial y}\right)^2\right] \quad (30)$$

where $\vec{E}$ is the electrical intensity. The substance properties, such as thermal conductivity k_l and specific heat capacity C_l, are assumed to remain constant and taken as that of the electrolyte for convenience.

In solving the energy equation, the temperature at inlet, workpiece, and tool are specified, while the exit temperature is assumed to be fully developed.

2.4. *Direct method analysis*

The direct problem consists of identifying the workpiece position for a prescribed tool shape. Furthermore, the variation in effective electrolyte conductivity affects the workpiece shape, which is attributed to variations in both the volume fraction of hydrogen gas and the temperature of the electrolyte. The direct method analysis procedure is as follows.

2.4.1. *Mesh generation*

In ECM, the workpiece shape is irregular and changes continuously during the machining process. A good distribution of model points is necessary for calculating the electric potential gradient and the fluid field. A body-fitted coordinate transformation technique, where a Poisson equation is used to transform an irregular physical domain $(x - y)$ to a rectangular computational domain $(\xi - \eta)$ [22], is applied herein and generates a smooth grid distribution. A typical mesh is indicated in Figure 2.

2.4.2. *Electric potential*

In this study, the electric potential field is solved by finite element method (FEM) to reduce the CPU time. The Galerkin residual equation for the governing equation of the electric field can be derived from Equation 1 as

$$\iint \left[\frac{\partial}{\partial x}\left(K_e \frac{\partial \phi}{\partial x}\right) + \frac{\partial}{\partial y}\left(K_e \frac{\partial \phi}{\partial y}\right)\right] \varphi(x,y)\,\mathrm{d}x\,\mathrm{d}y = 0, \quad i = 1, 2, \ldots, 8 \quad (31)$$

where $\varphi(x,y)$ is the shape function or trial function [23]. The element type applied in the present simulation is a 2D, 8-nodal quadratic isoparametric quadrilateral element. The corresponding shape function is

$$\varphi(x,y) = a_1 + a_2 x + a_3 y + a_4 x^2 + a_5 xy + a_6 y^2 + a_7 x^2 y + a_8 xy^2 \quad (32)$$

By integrating Equation 31 by parts once, we can solve it, with boundary conditions of Equation 2, numerically for the electric potential distribution in the interelectrode gap.

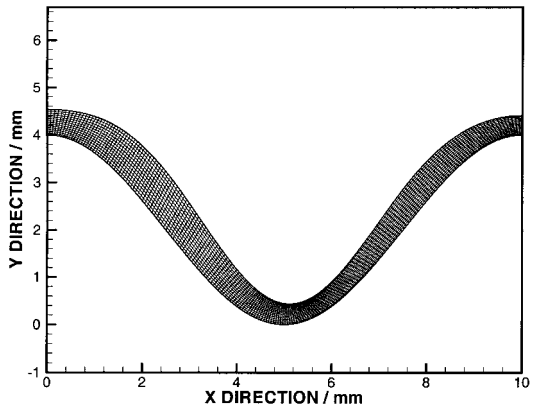

Fig. 2. A typical mesh used.

2.4.3. *Velocity/temperature/conductivity fields*

In calculating the two-dimensional two-phase thermal-fluid properties, a finite difference method is used to solve the partial differential equations.

The flow field is determined by the governing equations mentioned in Section 2.2. First, Equation 21 is employed to calculate the intermediate velocity field $(\alpha_i \mathbf{v}_i)^*$ with the corresponding initial parameters. Equation 25 is then used to determine the pressure correction q and Equation 23 is used to calculate $(\alpha_i \mathbf{v}_i)^{n+1}$. Furthermore, Equation 26 is used to calculate the volume fraction. The above procedure is repeated until the variation of the pressure correction q at each single node is less than 10^{-5}. Here the time represents the fictitious time of the iteration step in the numerical scheme.

The temperature field is determined by Equation 33. The convergence criteria refer to a situation in which the variation of the temperature at each single point is less than 10^{-4}.

Afterward, the electric conductivity can be calculated as the gas volume fraction and the temperature values when incorporated into Equation 7.

2.4.4. *Workpiece shape*

The workpiece shape can be obtained by Equation 4. The new positions (x_p, y_p) after Δt machining time are as follows:

$$x_{\mathrm{P}} = x_0 + \left[\frac{\Lambda \lambda_{\mathrm{a}} J}{\rho_{\mathrm{a}}} - f_{\mathrm{r}} \cos\theta\right] \times \Delta t \times \sin\theta \tag{34}$$

$$y_{\mathrm{P}} = y_0 + \left[f_{\mathrm{r}} \cos\theta - \frac{\Lambda \lambda_{\mathrm{a}} J}{\rho_{\mathrm{a}}}\right] \times \Delta t \times \cos\theta \tag{35}$$

where (x_0, y_0) represent the positions of the workpiece in the previous time step.

Steps 2.4.1 to 2.4.4 are repeated until the interelectrode gap reaches equilibrium. Namely, the relative variation at each single node in the consecutive time step is less than 10^{-4}.

2.5. *Inverse method analysis*

In the direct method, even if the influence of the thermal-fluid properties on ECM is considered, the workpiece shape for a given tool shape can be numerically predicted in an efficient manner. Therefore, the embedding method [17], which searches among the set of direct solutions for various tools until the required workpiece shape is found matched, is applied herein.

Assume that $a_1, a_2, \ldots, a_m$ are the coefficients of a Fourier cosine series of degree m associated with any given tool shape. Where $f(x)$ and $b_1, b_2, \ldots, b_m$ are those associated with the workpiece shape $h(x)$ resulting from $f(x)$ by the direct method. Finally, $c_1, c_2, \ldots, c_m$ are the coefficients of a Fourier cosine series of degree m associated with the required workpiece shape $r(x)$.

If $[A]$ is equivalent to $(a_1, a_2, \ldots, a_m)^{\mathrm{T}}$ with similar expressions applicable to $[B]$ and $[C]$, then the numerical iteration can be written as [17]

$$[A]^{k+1} = [A]^k + [\Delta A]^k \tag{36}$$

and

$$[\Delta A]^k = \left([C] - [B]^k\right) \cdot [J_{\mathrm{a}}]^{-1} \tag{37}$$

where k is the iteration counter, J_{a} is the Jacobian, and its (i, j) th element is represented by

$$\frac{\partial b_i}{\partial a_j} \simeq \frac{1}{\varepsilon}\left[b_i\left(a_1^k, \ldots, a_j^k + \varepsilon, \ldots, a_m^k\right) - b_i\left(a_1^k, \ldots, a_j^k, \ldots, a_m^k\right)\right], \quad j = 1, 2, \ldots, m. \tag{38}$$

where $\varepsilon = 10^{-3}$ is used herein. For each coefficient b_i, the direct method must be applied $(m+1)$ times for obtaining $b_i(a_1^k, \ldots, a_j^k, \ldots, a_m^k)$ and each $b_i(a_1^k, \ldots, a_j^k + \varepsilon, \ldots, a_m^k)$. Hence, the procedure could be extremely costly for a large m, and a proper value of m should be chosen.

The coefficients of the workpiece shape function can be obtained by the curve fitting method. Herein, $h(x)$ is approximated by the Fourier cosine series as

$$h(x) = \sum_{i=0}^{m} b_i \varphi_i(x) \tag{39}$$

where $\varphi_i(x)$ are constructed by both even and odd harmonics to increase the accuracy, that is,

$$\varphi_i(x) = \cos(\mathrm{i}\pi x / L) \tag{40}$$

where L is the length of the electrode in x-direction.

The coefficients of $h(x)$ are determined by the least-square method, in which the square difference between the required workpiece shape $r(x)$ is

$$ERR(h) = \sum_{k=1}^{n} [h(x_k) - r(x_k)]^2 \tag{41}$$

Since $ERR(h)$ is a function of b_i, the coefficients b_i can be solved by

$$0 = \frac{\partial ERR(h)}{\partial b_i} = \sum_{k=1}^{n} 2[h(x_k) - r(x_k)] \times \frac{\partial}{\partial b_i}[h(x_k) - r(x_k)] \tag{42}$$

or

$$\sum_{i=0}^{m} b_i \left[\sum_{k=1}^{n} \varphi_i(x_k)\varphi_j(x_k)\right] = \sum_{k=1}^{n} \left[r(x_k) \cdot \varphi_j(x_k)\right] \tag{43}$$

3. Numerical procedure

All numerical calculations are performed on a personal computer with an INTEL Pentium III 450 MHz processor. Notably, the normal CPU time for a direct method with a grid size of 201×15 is about 3660 s. The numerical procedure is as follows:

(i) Give the required workpiece shape and the machining conditions.
(ii) Apply the direct method to calculate the new shape of the workpiece until the interelectrode gap reaches equilibrium.
(iii) Calculate the coefficients of the workpiece shape by the curve fitting method.
(iv) Employ the embedding method to correct the tool shape, and repeat step (ii) to (iii) until the corrected term $[\Delta A]$ is less than 10^{-4}.

The tool shape obtained in step (iv) is evaluated by the relative error defined as

$$RERR = AERR/g_e = \left[\frac{1}{n}\sum_{k=1}^{n}(\Delta y_k)^2\right] \Big/ g_e \qquad (44)$$

where Δy_k is equal to $r(x_k) - y_k$ at each node k, and $r(x_k)$ is the required workpiece shape as stated above, while y_k is the workpiece shape if machined by the calculated tool shape.

4. Results and discussion

Tables 1 and 2 list the machining conditions and the electrolyte properties used herein, respectively. According to Figure 3, the numerical predictions by various models are in good qualitative agreement with the experimental data [24]. In particular, the result obtained from the two-dimensional two-phase model is closer to the experimental data than other results obtained by using the one-dimensional two-phase model. In the one-dimensional model, the volume fraction of the hydrogen gas, the most important thermal-fluid parameter for ECM [18], is almost linearly distributed from electrolyte entrance to exit. Therefore, the interelectrode gap thickness decreases linearly from electrolyte entrance to exit. However, in a two-dimensional two-phase model, the detailed distribution of the volume fraction of the hydrogen gas phase can be obtained so that the result is closer to the experimental data. Thus, the two-dimensional two-phase model is used to simulate the thermal-fluid properties properly, thus yielding an accurate prediction in electrochemical machining.

Table 1. Working conditions of electrochemical machining

Fig. no.	2	3, 4	11	12
Tool feed rate 10^{-6}, f_r/m s^{-1}	9.27	9.05	9.05	9.05
Applied voltage, ϕ_a/V	19.5	18.5	18.5	18.5
Temperature at entrance, T_0/K	297.5	297.5	297.5	297.5
Electrolyte flow flux 10^{-6}, Q/m^2 s^{-1}	1750	1750	3500	1750
Electrochemical equivalent 10^{-5}, λ_a/g C^{-1}		9.3161		
Metal density, ρ_a/kg m^{-3}		2698		
Current efficiency, Λ/%		92.5		

Table 2. Physical properties of the electrolyte ($NaCl + H_2O$) and the hydrogen gas

Electrolyte conductivity, K_{e0}/Ω^{-1} m^{-1}	7
Electrolyte liquid density, ρ_l/kg m^{-3}	1027
Hydrogen gas density 10^{-3}, ρ_g/kg m^{-3}	81.85
Specific heat capacity 10^3, C_l/J kg^{-1} K^{-1}	4.18
Thermal constant, γ/K^{-1}	0.016
Electrolyte liquid viscosity coefficient 10^{-3}, μ_l/kg m^{-1} s^{-1}	0.781
Hydrogen gas viscosity coefficient 10^{-6}, μ_g/kg m^{-1} s^{-1}	8.963
Thermal conductivity, k_l/W m^{-1} K^{-1}	0.63

Consider a desired workpiece shape represented by $r(x) = 2 + 2.0\cos(\pi x/5)$ with a feature that the shape is symmetric against the center axis through $x = 5$. The tool shape designed only by Fourier even harmonics [18] is also symmetric as shown in Figure 4. However, the workpiece machined by this tool shape is not symmetric. The fact that the fluid and thermal properties are not symmetric in the inlet and exit regions accounts for the metal removal rate is not being the same in these regions. Therefore, the use of only even harmonics for the electrode representation [18] leads to a large relative error and is no longer valid in the two-dimensional investigation. Conversely, the relative error for the case with even and odd harmonics is relatively small as listed in Table 3. Furthermore, the calculation time of the latter case does not increase owing to use of the same terms of $m = 5$.

Figure 5 illustrates that, as the desired workpiece is steep, the effect of the thermal-fluid is large. Thus, the predicted tool shapes behind the center using the two-dimensional model and the one-dimensional model [18] differ statistically from each other. This difference is owing to the fact that the varying curvature of the electrodes affects the electrolyte flow. The hydrogen gas

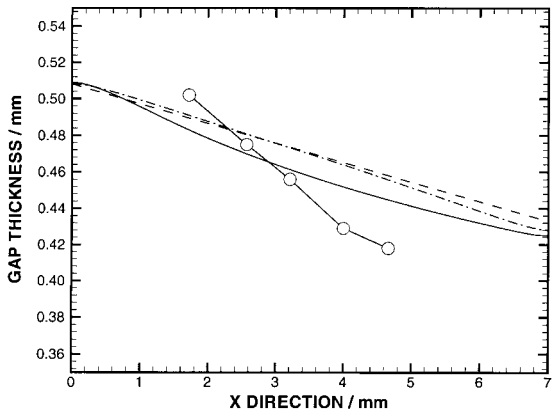

Fig. 3. Comparisons of workpiece shape between numerical and experimental results. (○) Experimental data [23]; (- - - - -) J. Hopenfeld and R.R. Cole; (- · - · - · -) one-dimensional two-phase model [18]; (——) two-dimensional two-phase model.

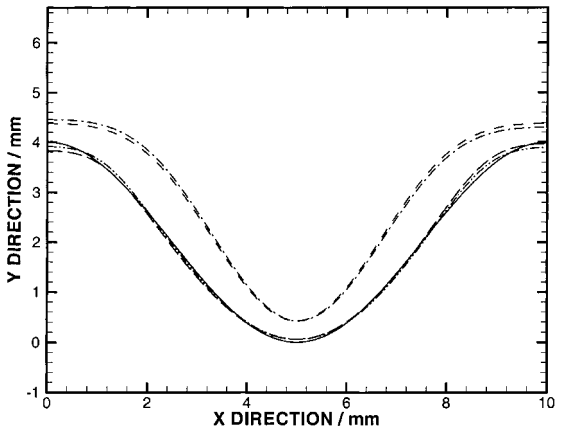

Fig. 4. Predicted tool shapes and corresponding workpiece shapes for different curve fitting functions. Desired workpiece shape is $r(x) = 2.0 + 2.0\cos(\pi x/5)$. (- - - - -) Tool shape using $\varphi_i(X) = \cos(2i\pi X/L)$ [18] (tool 1); (- · - · - ·) tool shape using $\varphi_i(x) = \cos(i\pi x/L)$ (tool 2); (– – –·) workpiece shape obtained from tool 1;(– · · – ·) workpiece shape obtained from tool 2; (——) desired workpiece shape.

Table 3. Relative errors of the workpiece for various machining conditions

Figure	Numerical model	m	Relative error/(%)
4	$\varphi_i(x) = \cos(2i\pi x/L)$	5	0.6000
4	$\varphi_i(x) = \cos(i\pi x/L)$	5	0.4041
5	One-dimensional	5	0.4041
5	Two-dimensional	5	0.2969
12	One-dimensional	5	0.4041
12	Two-dimensional	5	0.3580
13	One-dimensional	5	0.1868
13	Two-dimensional	5	0.2249

phase near the cathode is then concentrated downstream of the centre and is not effectively carried out by the electrolyte, as shown in Figure 6.

Figures 7 and 8 display the flow fields of the electrolyte liquid phase and the hydrogen gas phase, respectively. In Figure 7, the flow rate $\alpha \boldsymbol{v}$ of the electrolyte downstream of the centre is obviously small in the region near the cathode behind the center. However, the flow rate of the hydrogen produced by the electrochemical reaction increases along the flow direction and accumulates near the cathode, as shown in Figure 8.

The pressure distribution of the fluids (Figure 9) can be used to further elucidate the concentrating phenomenon. Since the flow field is significantly changed, a low-pressure region is formed in the centre of the interelectrode cell. The pressure then increases along the flow direction and decreases slightly at the exit. This pressure distribution causes the hydrogen gas to be trapped in this low-pressure region.

Figure 10 shows the temperature distribution. The temperature of the fluids increases along the flow direction due to the effect of the Joule law. Nevertheless, the temperature of the fluids near the cathode behind the centre is lower due to the gas concentration. The heat transfer capability of the gas phase is inferior to that of the liquid phase. The temperature near the workpiece is also higher for the above reason.

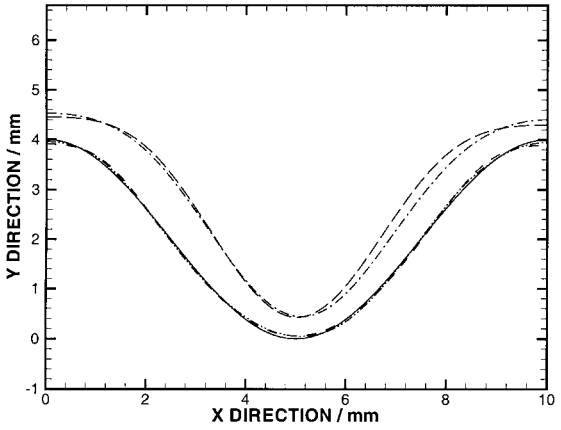

Fig. 5. Predicted tool shapes and corresponding workpiece shapes for different thermal-fluid models. The desired workpiece shape is $r(x) = 2.0 + 2.0\cos(\pi x/5)$ and the flow rate of the inlet electrolyte is 1750 mm s^{-1}. (- - - - -) Tool shape using one-dimensional model [18] (tool 1); (- · - · - ·) tool shape using two-dimensional model (tool 2); (– – –·) workpiece shape obtained from tool 1; (– · · – ·) workpiece shape obtained from tool 2; (——) desired workpiece shape.

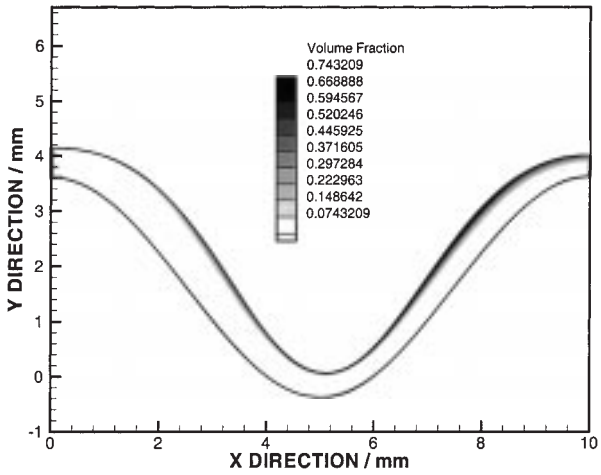

Fig. 6. Volume fraction distribution of hydrogen gas in equilibrium.

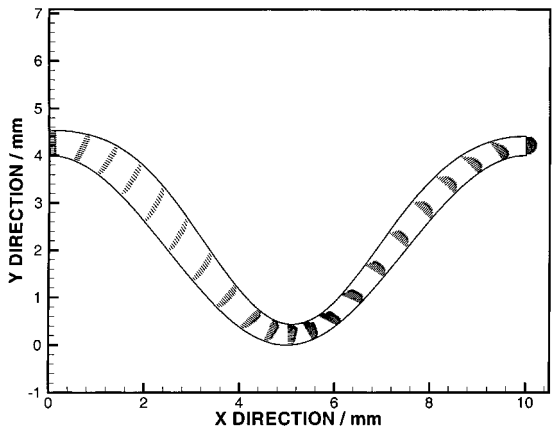

Fig. 7. Electrolyte velocity distribution in equilibrium (→) Unit vector: 3000 mm s^{-1}.

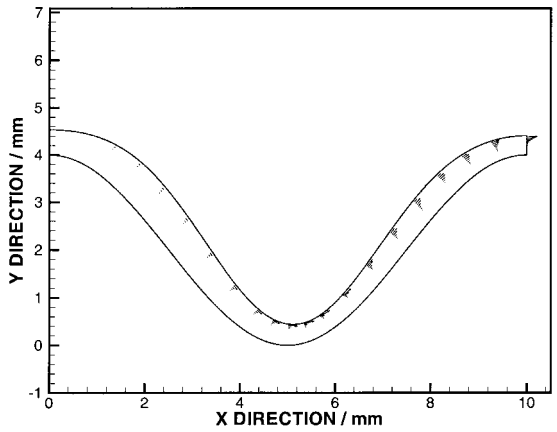

Fig. 8. Hydrogen velocity distribution in equilibrium (→) Unit vector: 3000 mm s^{-1}.

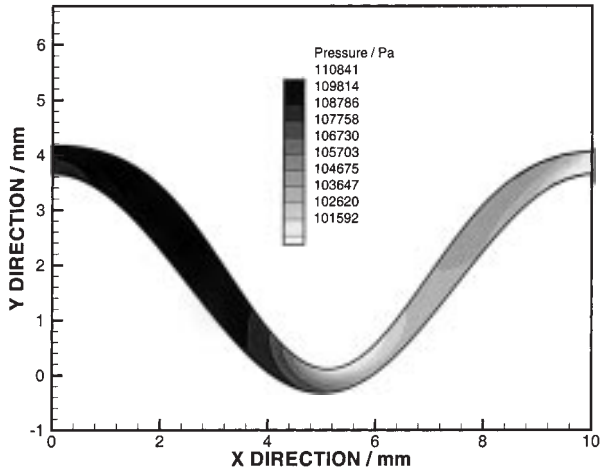

Fig. 9. Pressure distribution in equilibrium.

Figure 11 plots the variations of average temperature, void fraction and electrical conductivity in the section perpendicular to the flow direction against the flow

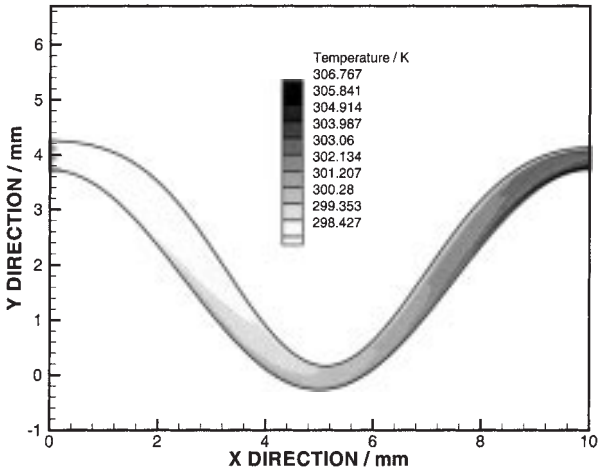

Fig. 10. Temperature distribution in equilibrium.

distance. As mentioned in Equation 7, the electrical conductivity decreases when either reducing the temperature or increasing the void fraction. Since the void fraction dominates in this case, the electrical conductivity varies with it. Thus, the predicted tool shapes by the one-dimensional model [18] and the two-dimensional model differ from each other. If the curvature of the electrode shape varies markedly, the flow is two-dimensional and the two-dimensional model should be used in the simulation. In this case, a one-dimensional model cannot obtain the detail of the gas phase distribution.

If the flow rate of the inlet electrolyte is increased, the two-dimensional nature of the flow is reduced but only slightly. According to Figure 12, the flow rate at the inlet is 3500 $m^2\ s^{-1}$, in which the predicted tool shapes using one-dimensional [18] and two-dimensional models still differ from each other. However, the difference is smaller than that in the case of 1750 $m^2\ s^{-1}$ as shown in Figure 5.

According to Figure 13, the desired workpiece shape is changed to $r(x) = 2 + 1.5\cos(\pi x/5)$. Therefore, the

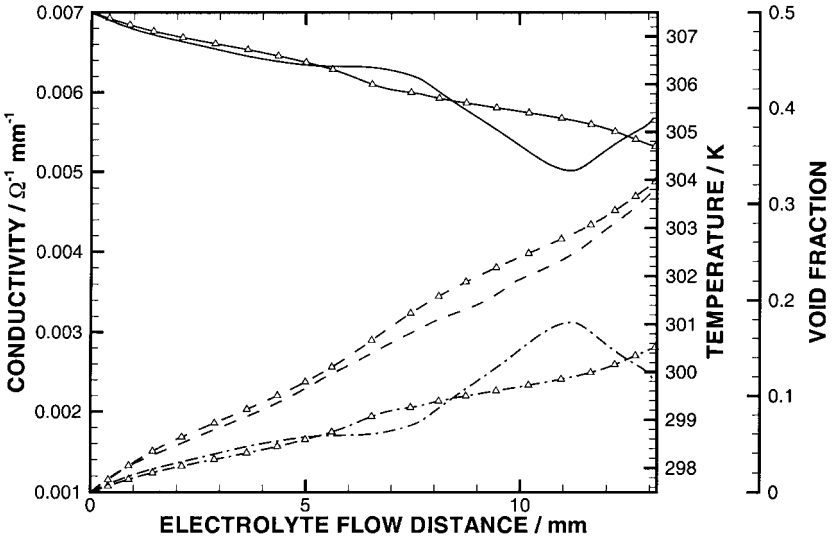

Fig. 11. Variation of void fraction, temperature and electrical conductivity along the stream path for different thermal-fluid models. Void fraction: (- · -△- · -) one-dimensional model [18]; (- · - · -) two-dimensional model. Temperature: (- -△- -) one-dimensional model [18]; (- - - -) two-dimensional model. Electrical conductivity: (–△–) one-dimensional model [18]; (——) two-dimensional model.

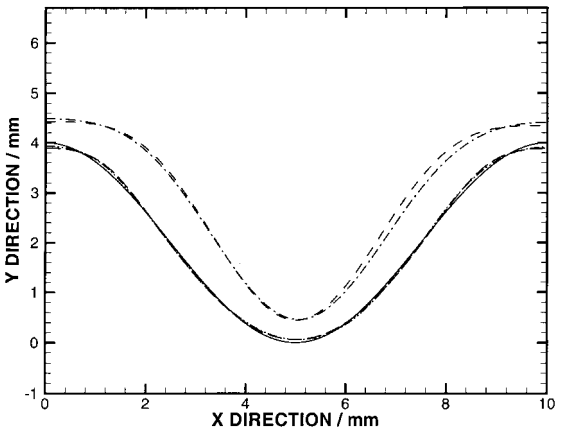

Fig. 12. Predicted tool shapes and corresponding workpiece shapes for different thermal-fluid models. Desired workpiece shape is $r(x) = 2.0 + 2.0\cos(\pi x/5)$ and the flow rate of the inlet electrolyte is 3500 mm s^{-1}. (- - - - -) Tool shape using one-dimensional model [18] (tool 1); (- · - · - ·) tool shape using two-dimensional model (tool 2); (– – – ·) workpiece shape obtained from tool 1; (– · · – · ·) workpiece shape obtained from tool 2; (——) desired workpiece shape.

curvature of the electrode shape varies only slightly. The two-dimensional nature of the flow is insignificant, accounting for the fact that the results of the one-dimensional model [18] and the two-dimensional resemble each other.

5. Conclusions

This work employs a numerical method with two-dimensional two-phase thermal-fluid analysis to predict a tool shape for a required workpiece shape in electro-chemical machining. Simulation indicates that the approximation of symmetry, that is only using even harmonics, is no longer valid in a two-dimensional investigation.

The effect of the two-dimensional thermal-fluid properties should be considered in the inverse method. If the curvature of the electrode shape varies widely, the two-dimensional phenomenon of the flow is apparent, and the two-dimensional model should be used in the simulation.

Although electrolyte with large flow rate can slightly reduce the effect of the thermal-fluid properties, the two-dimensional phenomenon still persists as the electrode shape is steep.

As the curvature of the electrode shape varies slightly, we recommend the use of one-dimensional analysis which uses less computational time and leads to accurate thermal-fluid properties.

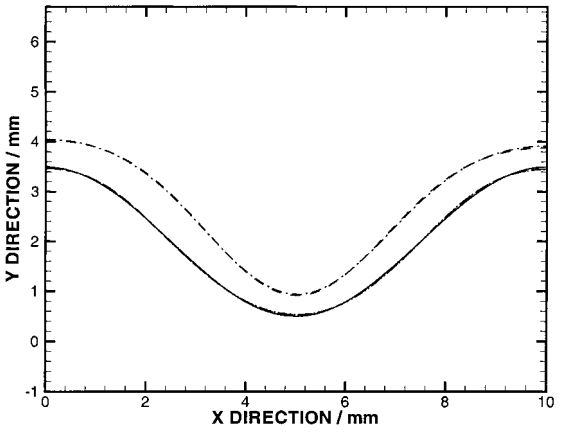

Fig. 13. Predicted tool shapes and corresponding workpiece shapes for different thermal-fluid models. Desired workpiece shape is $r(x) = 2.0 + 1.5\cos(\pi x/5)$ and the flow rate of the inlet electrolyte is 1500 mm s^{-1}. (- - - - -) Tool shape using one-dimensional model [18] (tool 1); (- · - · - ·) tool shape using two-dimensional model (tool 2); (- - - ·) workpiece shape obtained from tool 1; (– · · – · ·) workpiece shape obtained from tool 2; (——) desired workpiece shape.

References

1. J.A. Mcgeough, 'Principles of Electrochemical Machining' (J. Wiley & Sons, New York, 1974).
2. V.K. Jain and K.P. Rajurkar, *Precision Eng.* **13** (1991) 111.
3. A.L. Krylov, *Soviet Phys. Doklady* **13** (1968) 15.
4. P. Lawrence, PhD thesis, Leicester University, UK (1977).
5. D.E. Collett, R.C. Hewson-Brown and D.W. Windle, *J. Eng. Math.* **4** (1970) 29.
6. V.K. Jain and P.C. Pandey, *Precision Eng.* **2** (1980) 195.
7. M.B. Nanayakkare, PhD thesis, University of Strathclyde, UK (1977).
8. V.K. Jain and P.C. Pandey, *Int. J. Mach, Tool Des. Res.* **22** (1982) 341.
9. J.F. Thorpe and R.D. Zerkle, *Int. J. Math. Tool Des. Res.* **9** (1969) 131.
10. J.F. Thorpe and R.D. Zerkle, *in* C.L. Faust (Ed), 'Fundamentals of Electrochemical Machining' (The Electro-chemical Society, Princeton, NJ, 1971), p. 1.
11. V.K. Jain, P.G. Yogindra and S. Murugan, *Int. J. Mach. Tools Manufact.* **27**(1) (1987) 113.
12. L.W. Hourng and C.S. Chang, *J. Appl. Electrochem.* **23** (1993) 316.
13. L.W. Hourng and C.S. Chang, *J. Appl. Electrochem.* **24** (1994) 1170.
14. S. Das and A.K. Mitra, *Int. J. Num. Methods Eng.* **35** (1992) 1045.
15. A.A. Lacey, *J. Inst. Math. Applic.* **34** (1985) 259.
16. R. Hunt, *J. Comp. Phys.* **65** (1986) 448.
17. R. Hunt, *Int. J. Num. Methods Eng.* **29** (1990) 1177.
18. C.S. Chang, L.W. Hourng and C.T. Chung, *J. Appl. Electrochem.* **29** (1999) 321.
19. M.B. Carver, *J. Fluid Eng.* **106** (1984) 147.
20. A.W. Bush and G.S. Marshall, 'Flow Modelling in Industrial Processes' (Ellis Horwood, Chichester, West Sussex, England, 1989), p. 164.
21. R. Peyret and T.D. Taylor, 'Computational Methods for Fluid Flow' (Springer, New York, 1983).
22. J.P. Thompson, F.C. Thames and C.W. Mastin, *J. Comput. Phys.* **24** (1977) 274.
23. D.S. Burnett, 'Finite Element Analysis From Concepts to Application' (Addison-Wesley, Singapore, 1987).
24. J. Hopenfeld and R.R. Cole, *J. Eng. Industry* Aug. (1969) 755.